Simultaneous Mobile Information and Power Transfer by Resonant Beam

Mingqing Liu, Hao Deng, Qingwen Liu, *Senior Member, IEEE*, Jie Zhou, Mingliang Xiong, Liuqing Yang, *Fellow, IEEE*, and Georgios B. Giannakis, *Fellow, IEEE*

***Abstract*—Simultaneous lightwave information and power transfer (SLIPT) has been regarded as one of the enabling technologies to enhance the battery-life and data-rate for mobile electronics in the Internet of things (IoT). The existing SLIPT schemes face the challenge of achieving narrow beam transmission and mobile receiver positioning simultaneously. In this paper, we propose a simultaneous mobile information and power transfer (SMIPT) approach using the energy-concentrated resonant beam, which can realize self-alignment with the mobile receiver. To reveal the mobility mechanism of SMIPT, we present a geometric model of the mobile transmission channel and an analytical model of mobile energy and information transfer. Refraction is ignored in the geometric model and Fresnel/paraxial approximations are adopted in the above analytical model. Numerical evaluation illustrates that the exemplary SMIPT system can deliver 5 W charging power and enable 9.5 bps/Hz spectral efficiency with the moving range of 40-degree field of view (FOV) over 3 m distance. Thus, SMIPT exhibits a viable solution of simultaneous narrow beam transmission and mobile receiver positioning for high-power and high-rate SLIPT.**

***Index Terms*—Simultaneous mobile information and power transfer, wireless power transfer, mobility and self-alignment, retro-reflective resonator.**

I. Introduction

NEXT-GENERATION networks are expected to support the significant growth of energy consumption and data transmission for billions of wireless devices due to the advancement of the IoT, where simultaneous wireless information and power transfer (SWIPT) appeals as one of the enablers [1]. However, due to the growing spectrum crisis, the SLIPT based on visible/infrared light has become a potential alternative to SWIPT based on radio frequency (RF) signals [2], [3]. The SLIPT has two classes: 1) omni-directional SLIPT generally with an LED transmitter sacrifices transmission efficiency for wide coverage [4]–[8], thus the deliverable power is usually at mW level, limiting the application scenarios; and 2) directional SLIPT based on lasers faces the challenge of mobile receiver positioning using the narrow electromagnetic beam [9], [10], then the mechanical alignment is required with a high-power transfer, increasing the practical difficulties. Thus, the conflict between narrow beam transmission and mobile receiver positioning is the dilemma for SLIPT system design. In this paper, we present an SMIPT approach using the resonant beam to deal with the above issue. The SMIPT is capable of offering multi-Watt power and high-efficiency data transfer to mobile devices with self-alignment capability in a room-size environment as in Fig. 1.

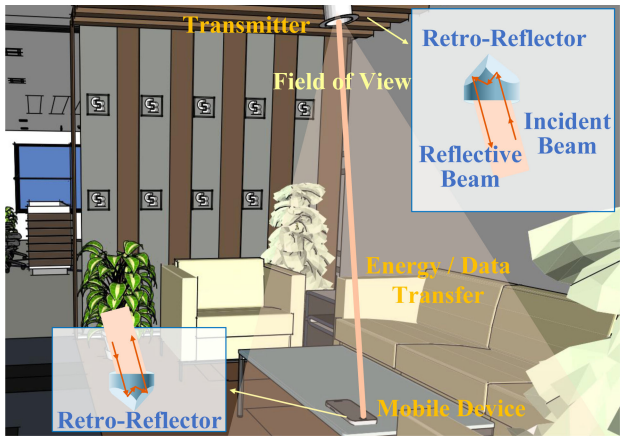

Fig. 1. SMIPT application scenario.

The SMIPT relies on the resonant beam system (RBS) for information and energy transfer. RBS uses an open-cavity laser resonator to provide high-efficiency SLIPT [11]–[13]. In the RBS, a transmitter consists of a high-reflective mirror and a gain medium, and a receiver consists of an output coupling mirror and a Photovoltaic (PV) cell. The transmitter and receiver are spatially separated to form a resonator. The resonant beam generated within the resonator acts as the energy and information carrier. The RBS brings the following advantages: 1) the resonant beam transmission is energy-concentrated similar to directional SLIPT; and 2) the resonant beam ceases immediately and automatically in case of foreign object invasion, which leads to the unique safety feature [14]. Therefore, the SMIPT inherits the features of RBS, in terms of high-power energy-concentrated

Manuscript received October 20, 2020; revised March 16, 2021; accepted April 26, 2021. Date of publication May 7, 2021; date of current version May 26, 2021. The associate editor coordinating the review of this manuscript and approving it for publication was Prof. Youngchul Sung. The work was supported in part by the National Key R&D Program of China under Grants 2020YFB2103900 and 2020YFB2103902, and in part by the National Natural Science Foundation of China under Grants 61771344 and 62071334. *(Corresponding authors: Qingwen Liu; Hao Deng.)*

Mingqing Liu, Qingwen Liu, Jie Zhou, and Mingliang Xiong are with the College of Electronics and Information Engineering, Tongji University, Shanghai 201804, People's Republic of China (e-mail: clare@tongji.edu.cn; qingwen.liu@gmail.com; jzhou@tongji.edu.cn; xiongml@tongji.edu.cn).

Hao Deng is with the School of Software Engineering, Tongji University, Shanghai 201804, China (e-mail: denghao1984@tongji.edu.cn).

Liuqing Yang and Georgios B. Giannakis are with the Department of Electrical and Computer Engineering, University of Minnesota, Minneapolis, MN 55455 USA (e-mail: qingqing@umn.edu; georgios@umn.edu).

Digital Object Identifier 10.1109/TSP.2021.3077799

1053-587X © 2021 IEEE. Personal use is permitted, but republication/redistribution requires IEEE permission.
See https://www.ieee.org/publications/rights/index.html for more information.

Authorized licensed use limited to: Wenzhou University. Downloaded on June 15,2021 at 09:28:02 UTC from IEEE Xplore. Restrictions apply.

beam transmission over the air, with the premise of guaranteeing safety.

As in Fig. 1, retro-reflector can reflect the incident beam from arbitrary direction back parallel to the original direction, and the typical structures are corner cube reflector (CCR) [15], [16], cat's eye [17], etc. Adopting retro-reflectors at both ends of the spatially separated resonator enables SMIPT with self-alignment capability. As a result, energy-concentrated resonant beam can be sent to the mobile receiver even if it changes the position within the coverage of SMIPT.

The mobility of RBS has been discussed in [11]. However, the mechanism of its self-alignment has not been analyzed and the quantitative effects on SMIPT performance have not been well studied. Thus, we investigate here the mobility mechanism and establish an analytical model of SMIPT.

In this paper, we at first introduce the SMIPT system architecture and build a geometrical model of the mobile transmission channel. Afterwards, we adopt the resonator mode analysis and laser output power model to establish the analytical model for mobile energy transfer. Then, we can obtain the output laser power under the arbitrary moving status of the remote CCR inside the receiver. Adopting the PV for energy harvesting and avalanche photodiode (APD) for information reception, we finally evaluate the energy and data transfer performance within the receiver's moving range. We numerically demonstrate that the SMIPT system can deliver 5 W wireless charging power and enable 9.5 bps/Hz spectral efficiency of data transfer simultaneously, and allows receivers to move within 3 m and 40-degree FOV.

The contributions of this manuscript are:

1) The proposed SMIPT can simultaneously achieve high-power transfer and self-alignment within large FOV, which overcomes the conflict between narrow beam transmission and mobile receiver positioning with the existing SLIPT schemes.
2) We establish a geometric model of mobile transmission channel in SMIPT, where the self-alignment mechanism with the receiver's 6 degrees of freedom for movement can be revealed.
3) We propose an analytical model of energy and information transfer, where the moving range (FOV and distance), charging power, and spectral efficiency can be quantitatively evaluated.

The remainder of this paper is organized as follows. In Section II, we propose the SMIPT scheme and describe its architecture and principle. In Section III, we introduce the geometry of a resonator with two identical CCRs and derive a geometric model of the mobile transmission channel. Afterwards, we establish an analytical model of mobile energy and information transfer in SMIPT and the analysis method of power and data transfer performance in Section IV. In Section V, we demonstrate the moving range, the charging power, and the spectral efficiency through numerical analysis. Finally, we make a conclusion in Section VI.

To estimate the transmission channel loss of the proposed system, we use the wave optics method to stimulate the field transmission and the geometric optics method to analyze the self-alignment characteristic. It should be stated that the Fresnel approximation and paraxial approximation are applied in calculating the field distribution, and we adopt the method of determining the Gaussian spot radius to approximate the size of the beam cross section in the resonator. Besides, the refraction of optical devices such as CCR is neglected.

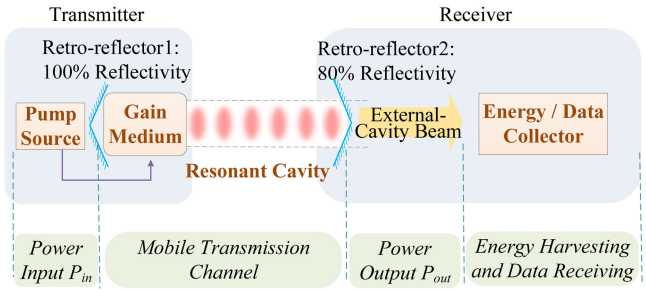

Fig. 2. SMIPT structure and energy flow.

II. System Overview

As in Fig. 2, we present an exemplary system design to illustrate the principle and characteristics of the SMIPT approach. SMIPT system consists of a transmitter and a receiver. The spatially separated transmitter and receiver jointly form a laser resonator. The SMIPT system includes the following key components: i) pump source, ii) gain medium, iii) energy and data collector, and iv) double-retroreflective resonant cavity.

The transmitter is comprised of a pump source, a gain medium, and a retro-reflector with 100% reflectivity. Similar to the RF amplifier, the pump source provides energy for the gain medium to stimulate light radiation. The gain medium is usually a thin disk to amplify optical power.

The receiver consists of the energy and data collector and a retro-reflector. The retro-reflector is partially reflective, e.g., 80% reflectivity, which acts as an output coupler allowing the resonant beam to pass through and yielding a laser beam. The laser beam is split into two streams by an optic power splitter. One is sent to the PV and the other to the APD for energy harvesting and information receiving, respectively.

The double-retroreflective resonant cavity enables mobility. Due to the retroreflective characteristic of the retro-reflector, the stimulated light can be reflected back and forth within the cavity even as the two reflectors are not strictly facing each other. If the light magnification can compensate for the transmission loss inside the cavity and power output at the output coupler (i.e., the retro-reflector at the receiver), the stable resonant beam can be formed.

Overall, the energy flow in SMIPT can be outlined as follows: i) P_{in} from pump source is input into the transmitter, contributing to stimulating resonant beam; ii) resonant beam transfers within the mobile transmission channel; iii) resonant beam is output as an extra-cavity beam with P_{out}; iv) the extra-cavity beam power output for energy harvesting and data receiving.

To figure out the mobility mechanism of SMIPT, we will at first present the geometric model of the mobile transmission channel, which is formed by the double-retroreflective resonant

Authorized licensed use limited to: Wenzhou University. Downloaded on June 15,2021 at 09:28:02 UTC from IEEE Xplore. Restrictions apply.

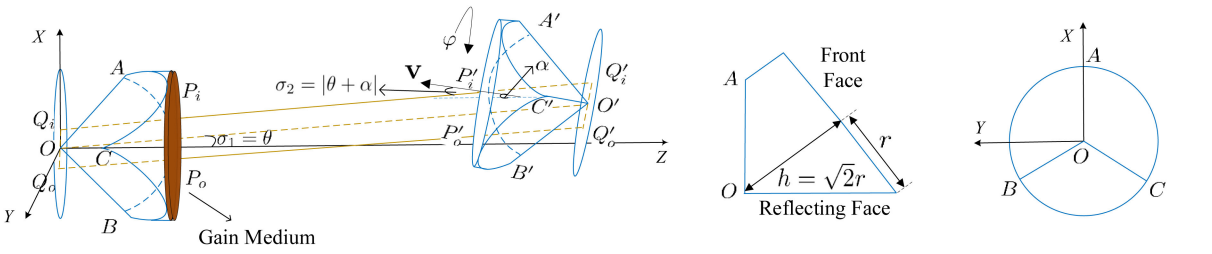

(a) Resonator with Two Corner-Cube Reflectors (b) Side View of Corner-Cube (c) Top View of Corner-Cube

Fig. 3. Geometric relationship of the two CCRs.

cavity. Afterwards, we can analyze the SLIPT performance by establishing the mobile energy and information transfer model relying on the above energy flow.

III. Geometric Model of Mobile Transmission Channel

Mobile transmission channel of SMIPT system is based on a double-retroreflective laser resonator. We investigate here a resonator with two CCRs and a thin-disk gain medium. After introducing the geometric properties of CCR, we prove that the double-retroreflective resonator is equivalent to a Fabry-Perot (FP) resonator, which justifies the mobility of the SMIPT.

A. Architecture and Parameters

As in Fig. 3(a), the resonator consists of two identical circular CCRs, and a thin-disk gain medium attached to the left CCR. The parameters of the two CCRs are depicted in Fig. 3(b), where r is the circular front face radius and $h = \sqrt{2}r$ is the height. Moreover, the size of the gain medium is identical to the CCR's front face. The coordinate system is established as in Fig. 3(c). The origin O is the vertex of the left CCR, and Z-axis is perpendicular to the left CCR's front face passing through its center.

The position of the left CCR is fixed, while the right CCR at the receiver can be arbitrarily moved with the six degrees of freedom. Specifically, the right CCR can be shifted along the X, Y, and Z axis, resulting in its vertex coordinates $O'(a, b, c)(a, b, c \in \mathbb{R}, c \geq 2\sqrt{2}r)$, where $\mathbb{R}$ represents the set of real numbers; and rotated around X, Y, Z axis with angles β_1, β_2, β_3, respectively. Thus, the movement of the right CCR can be expressed as the six degrees of freedom $(a, b, c, \beta_1, \beta_2, \beta_3)$.

In Fig. 3 (a), OO' is the vertex connection of two CCRs, and the length is L. $\mathbf{v}$ is the normal vector on the front face of the right CCR. Define θ as the pan angle between OO' and Z-axis, α as the tilt angle between $\mathbf{v}$ and Z-axis, and φ as the rotation angle that the right CCR rotates around $\mathbf{v}$. Their geometric relationship is depicted as follows according to the law of cosines in 3-dimension space [18]:

$$\begin{aligned} \cos\alpha &= \cos\beta_1 \cos\beta_2, \\ \varphi &= \beta_3. \end{aligned} \tag{1}$$

Thus, the six degrees of freedom can be reduced to four, i.e., $(a, b, c, \beta_1, \beta_2, \beta_3)$ can be represented by $(L, \theta, \alpha, \varphi)$, where $L := \sqrt{a^2 + b^2 + c^2}$, $\theta := \arccos(c/\sqrt{a^2 + b^2 + c^2})$, $\alpha := \arccos(\cos\beta_1 \cos\beta_2)$, and $\varphi := \beta_3$.

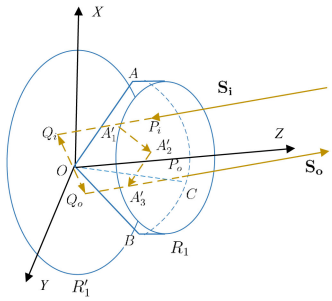

Fig. 4. Geometric relationship of incident and reflection rays by a CCR.

B. Geometrical Properties of a Perfect CCR

Geometrical properties of the perfect CCR are considered at first. The CCR is schematically represented in Fig. 4, and the refraction of CCR is ignored.

1) Retroreflection: Assume a ray $\mathcal{L}$ enters the CCR and intersects the front face at P_i along the direction described by

$$\mathbf{S_i} = (l, m, n), \tag{2}$$

where l, m, n are the direction cosine. $\mathcal{L}$ passes through the front face of CCR and impinges on a reflecting surface in XOZ with the intersection A'_1. Similarly, the reflected rays intersect the other two reflecting surfaces at A'_2 and A'_3, respectively. Finally, the ray after three reflections exits from CCR through P_o on the front face with the directional vector $\mathbf{S_o}$, where

$$\mathbf{S_o} = (-l, -m, -n). \tag{3}$$

Thus, the incident ray is parallel to the outgoing ray after reflections inside the CCR. The CCR has a retroreflective characteristic.

2) Path Length Inside the CCR: In Fig. 4, the front face of the CCR is marked as $\mathcal{R}_1$. Imagine a reference plane $\mathcal{R}'_1 || \mathcal{R}_1$ that passes through the vertex O. Then extend $P_i A'$ and $P_o A'_3$ to intersect plane $\mathcal{R}'_1$ at Q_i and Q_o. It has been verified that Q_i and Q_o are symmetric about O and the following equation has been verified in [16, Eq. (14)]:

$$|P_i Q_i| + |Q_o P_o| = |P_i A'_1| + |A'_1 A'_2| + |A'_2 A'_3| + |A'_3 P_o|. \tag{4}$$

It means that the path length inside the CCR of a ray from point P_i through A'_1, A'_2, A'_3 to point P_o, is equivalent to the ray passes from P_i through A'_1 to Q_i, experiences a displacement $Q_i Q_o$, and then propagates from Q_o through A'_3 to P_o. Among them, $Q_i Q_o$ doesn't contribute to the path length difference. $\mathcal{R}'_1$ can be regarded as an equivalent plane for field calculation [16].

Authorized licensed use limited to: Wenzhou University. Downloaded on June 15,2021 at 09:28:02 UTC from IEEE Xplore. Restrictions apply.

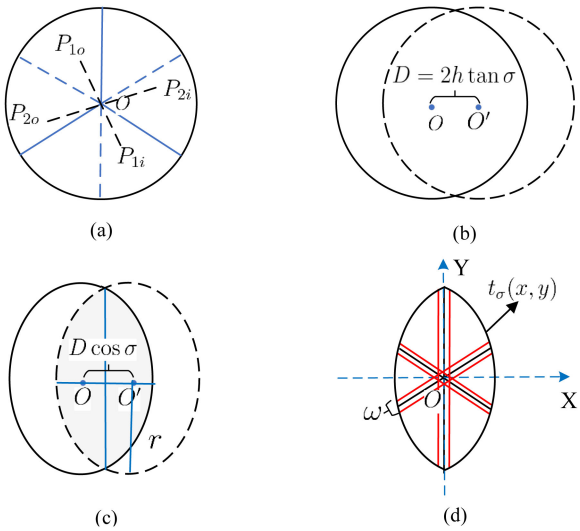

Fig. 5. The CCR's active reflecting area.

3) Active Reflecting Area: Fig. 5 depicts the top view of the CCR shown in Fig. 4 as seen from the front face. In Fig. 5 (a), a ray that incidents at point P_{1i} will be retroreflected from point P_{1o}, which is symmetric with P_{1i} about O. And the same movement happens to point P_{2i} and P_{2o}. For an incident beam consisting of countless rays, the shape of the retroreflected beam can be formed by moving each intersection of the ray at the CCR's front face to a symmetric position with respect to O. The shape of the CCR's front face is defined as the input aperture, while the shape of the retroreflected beam is called the output aperture. The overlapping area of the two apertures is called the active reflecting area of CCR, outside which the light will not be retroreflected [15].

When the incident beam is at normal incidence to the front face of CCR, the input aperture coincides with the output aperture. Otherwise, the center of output aperture will shift to O' as shown in Fig. 5 (b). As viewed from the front face, the offset distance $|OO'|$ between the output and the input aperture is defined as D, and D can be expressed as [15, Sec. 3]

$$D = 2h\tan\sigma, \tag{5}$$

where $h = \sqrt{2}r$ and σ is the angle between the incident beam and the normal vector $\mathbf{v}$.

When $D/2 \geq r$, the active reflecting area will reduce to zero. Then, we can obtain the maximum angle of the beam incidents on the CCR from (5) as

$$\sigma_{max} = \arctan(\frac{r}{h}) = 35.26^\circ. \tag{6}$$

However, as viewed from the incident beam, the distance D should multiply $\cos\sigma$ [15, Sec 2.6]. Thus, the active reflecting area for the beam incident at σ can be regarded as the overlap of two ellipses as shown in Fig. 5 (c). Moreover, for a real CCR, the edges formed by the intersection of each two reflecting surfaces cannot reflect beams [19]. In Fig. 5 (d), defining the edge width as ω, the area between two parallel red lines represents the edge of a CCR. We establish a coordinate system with the center of the active reflecting area for the origin O. We adopt the indication function to depict the reflective area by 1 and non-reflective area by 0. Then, the boundary function of the CCR's active reflecting area depending on the incident angle of the beam is

$$t_\sigma(x,y) = \begin{cases} 1, & \dfrac{(x + D\cos\sigma/2)^2}{M} + \dfrac{y^2}{N} \leq 1 \quad \text{and} \\ & \dfrac{(x - D\cos\sigma/2)^2}{M} + \dfrac{y^2}{N} \leq 1 \\ 0, & \dfrac{(x \pm D\cos\sigma/2)^2}{M} + \dfrac{y^2}{N} \geq 1 \\ 0, & -\dfrac{\sqrt{3}}{3}w < y \pm \dfrac{\sqrt{3}}{3}x < \dfrac{\sqrt{3}}{3}w \\ 0, & -\dfrac{w}{2} < x < \dfrac{w}{2} \end{cases}, \tag{7}$$

where $M := (r\cos\sigma)^2$ and $N := r^2$.

C. Equivalency Between Double-Retroreflective Resonator and Fabry-Perot Resonator

We analyze the situation where the incident angle of the resonant beam to the right CCR is below the maximum allowable incident angle of it. As shown in Fig. 3(a), the normal vector of the right CCR with arbitrary movement can be presented as $\mathbf{v} = (v_1, v_2, v_3)$, where $v_1 := \cos\beta_2$, $v_2 := \cos\beta_3$, $v_3 := \sqrt{1 - \cos^2\beta_2 - \cos^2\beta_3}$. The incident angle of the resonant beam to the right CCR can be defined as the angle between $\mathbf{v} = (v_1, v_2, v_3)$ and beam's vector in the coordinate system (a, b, c). Thus, the proof below is based on the following condition according to the geometric relationship [20, page 10, Eq. (2)]:

$$\arccos\left(\frac{v_1 a + v_2 b + v_3 c}{\sqrt{a^2 + b^2 + c^2}\sqrt{v_1^2 + v_2^2 + v_3^2}}\right) < \sigma_{max}. \tag{8}$$

1) Optical Axis Determination: A ray $\mathcal{L}$ from an arbitrary direction described by $\mathbf{S_i}(l, m, n)$, which is excited by the gain medium between two CCRs enters the left one at P_i, and intersects the equivalent plane of the left CCR at point $Q_i(x_i, y_i, 0)$. After the internal reflection of the CCR, the outgoing ray $\mathcal{L}_o$ intersects with the equivalent plane at $Q_o(-x_i, -y_i, 0)$. Then $\mathcal{L}_o$ enters the right CCR after passing through the free-space cavity and intersects with the equivalent plane of the right CCR at $Q'_o(lt - x_i, mt - y_i, nt)$, where $t = (v_1(x_i + a) + v_2(y_i + b) + v_3 c)/(v_1 l + v_2 m + v_3 n)$. Again after the internal reflections of the right CCR, the reflected ray travels at $Q'_i(2a - lt + x_i, 2b - mt + y_i, 2c - nt)$, which is symmetric with Q'_o about $O'(a, b, c)$.

After a round-trip transmission inside the resonator, $\mathcal{L}_o$ enters the left CCR again and intersects with the equivalent plane at Q_{i1}, which can be depicted as

$$Q_{i1}\left(2a - 2\frac{lc}{n} + x_i, 2b - 2\frac{mc}{n} + y_i, 0\right). \tag{9}$$

Similarly, we can derive that after k roundtrips, the intersection point of $\mathcal{L}$ and the equivalent plane of the left CCR is

$$Q_{ik}\left(2k(a - \frac{lc}{n}) + x_i, 2k(b - \frac{mc}{n}) + y_i, 0\right). \tag{10}$$

In order to keep $\mathcal{L}$ retroreflected within the resonator, the intersection point of the ray should still be within the active

Authorized licensed use limited to: Wenzhou University. Downloaded on June 15,2021 at 09:28:02 UTC from IEEE Xplore. Restrictions apply.

reflecting area of the left CCR when $k \to \infty$. So in (10), the following conditions need to be satisfied:

$$a - \frac{lc}{n} = 0, \quad b - \frac{mc}{n} = 0. \tag{11}$$

Then, we can obtain the following relationship from (11):

$$\mathbf{O}' \times \mathbf{S}_i = (bn - ma, lc - na, am - lb) = 0, \tag{12}$$

where $\mathbf{O}'(a, b, c)$ represents the vector of OO'. Therefore, any rays parallel with OO' can keep being reflected back and forth in the resonator. Moreover, the pair of retroreflected rays are symmetric about OO', which can be regarded as the optical axis of the resonator with arbitrary movement.

2) Round-Trip Path Length of All Rays Within Resonator: The following geometric relationships can be derived from (4) and (12) as

$$Q_i Q_i' \parallel Q_o Q_o' \parallel OO', \tag{13}$$

$$|Q_i Q_i'| + |Q_o Q_o'| = 2|OO'|. \tag{14}$$

Therefore, the path length of all rays which form a resonant beam reflected back and forth during a roundtrip in the resonator is $2|OO'|$. It means that the resonant beam generated in the resonator is parallel to and symmetric about the optical axis, even as the right CCR moves arbitrarily. Therefore, the double-retroreflective resonator is equivalent to an FP resonator composed of two plane mirrors perpendicular to OO'. Moreover, the size of the plane mirror is equal to the active reflecting area of the CCR.

3) Active Reflecting Areas of Reflectors in FP Resonator: The movement of the right CCR leads to the change of σ_1 and σ_2 that the resonant beam impinges on the left and right CCR, respectively. Moreover, σ_1 and σ_2 can be expressed in pan angle θ and tilt angle α. We discuss the relationship between θ and α with σ_1 and σ_2 below.

In Fig. 6, we simplify the 3-dimensional resonator in Fig. 3 to 2-dimension. We denote θ counterclockwise as positive and clockwise as negative; α counterclockwise as negative and clockwise as positive. As in Fig. 6, the typical movement of the right CCR can be summarized as follows:

(a) The right CCR turns counterclockwise around the left CCR by θ, and tilts clockwise by α. Then, for left CCR $\sigma_1 = \theta$, and for right CCR $\sigma_2 = (\theta + \alpha)$.

(b) The right CCR turns counterclockwise by θ, tilts counterclockwise by α, and $\alpha > \theta$. Then, for left CCR $\sigma_1 = \theta$, and for right CCR $\sigma_2 = (-\alpha - \theta)$.

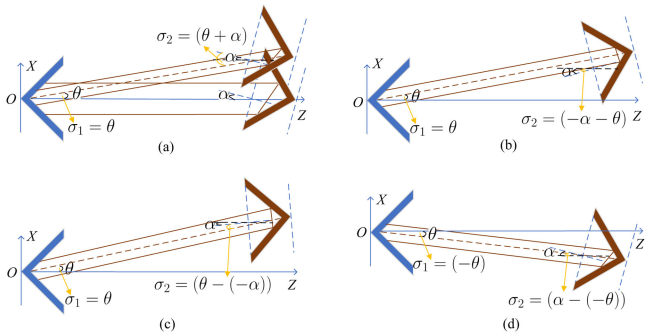

Fig. 6. A two-dimensional simplified model of a resonator with two CCRs.

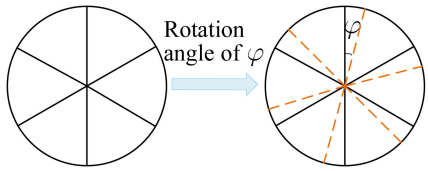

Fig. 7. The right CCR in the resonator with and without rotation angle φ.

(c) The right CCR turns counterclockwise by θ, tilts counterclockwise by α, and $\alpha < \theta$. Then, for left CCR $\sigma_1 = \theta$, and for right CCR $\sigma_2 = (\theta - (-\alpha))$.

(d) The right CCR turns clockwise by θ, and tilts clockwise by α. Then, for left CCR $\sigma_1 = (-\theta)$, and for right CCR $\sigma_2 = (\alpha - (-\theta))$. The other two cases are $\sigma_2 = (-\theta - \alpha)$ and $\sigma_2 = (-\theta + (-\alpha))$.

In summary, for left CCR, the incident angle of the resonant beam on it is

$$\sigma_1 = |\theta|, \tag{15}$$

and for right CCR

$$\sigma_2 = |\theta + \alpha|. \tag{16}$$

Furthermore, in Fig. 7, as the right CCR rotates around $\mathbf{v}$ by φ, the edges of the right CCR rotate by φ. Then, we obtain the expressions of the active reflecting areas at the two ends of the FP resonator with the right CCR's movement. For the left CCR, the active reflecting area can be expressed as (7) when $\sigma = \sigma_1$; and for the right CCR, the expression can be organized as (17) shown at the bottom of this page. The active reflecting areas are the essential factors to analyze the energy transfer in the SMIPT system, which will be discussed in Sec. IV.

$$t_{\sigma_2,\varphi}(x,y) = \begin{cases} 1, & \dfrac{(x + D\cos\sigma_2/2)^2}{M} + \dfrac{y^2}{N} \le 1 \quad \text{and} \quad \dfrac{(x - D\cos\sigma_2/2)^2}{M} + \dfrac{y^2}{N} \le 1 \\ 0, & \dfrac{(x + D\cos\sigma_2/2)^2}{A} + \dfrac{y^2}{B} \ge 1 \quad \text{or} \quad \dfrac{(x - D\cos\sigma_2/2)^2}{M} + \dfrac{y^2}{N} \ge 1 \\ 0, & -\dfrac{w}{2\cos(30^\circ + \varphi)} < y - \tan(30^\circ + \varphi)x < \dfrac{w}{2\cos(30^\circ + \varphi)} \\ 0, & \dfrac{w}{2\cos(150^\circ + \varphi)} < y - \tan(150^\circ + \varphi)x < -\dfrac{w}{2\cos(150^\circ + \varphi)} \\ 0, & \dfrac{w}{2\cos(90^\circ + \varphi)} < y - \tan(90^\circ + \varphi)x < -\dfrac{w}{2\cos(90^\circ + \varphi)} \end{cases}. \tag{17}$$

Authorized licensed use limited to: Wenzhou University. Downloaded on June 15,2021 at 09:28:02 UTC from IEEE Xplore. Restrictions apply.

IV. Analytical Model of Mobile Energy and Information Transfer

Obtaining the output power P_{out} of the SMIPT is the premise of analyzing its wireless charging power and wireless communication capability. We can calculate the output power based on the laser output power model as [21, Eq. (10.7)]:

$$P_{out} = A_b I_S \frac{(1-R)V}{1-RV^2+\sqrt{R}V\left[1/(V_S V)-V_S\right]} \times \left[g_0\ell - |\ln\sqrt{RV_S^2V^2}|\right], \tag{18}$$

where A_b is the overlapping area of resonant beam and gain medium, I_s is the saturated light intensity, $g_0\ell$ represents the small-signal gain, R is the reflectivity of the output coupler, and V_s and V depict the loss factors inside the gain medium and during intra-cavity transmission. Relying on the geometric model in Sec. III, we employ the resonator mode analysis to obtain V and A_b. We will specify the details in the following.

A. Power Input to the Transmitter

The power P_{in} input to the transmitter for pumping the gain medium is supposed to be converted to P_{avail}, which denotes the power at the upper laser level in the medium that is available in the form of inversion. P_{avail} ultimately contributes to the generation of stimulated radiation. This pump process can be depicted as follow with the excitation efficiency η_{excit} [21, Eq. (9.19)]:

$$P_{avail} = \eta_{excit} P_{in}, \tag{19}$$

where P_{in} is the input electrical power and η_{excit} is different with different pumping methods, such as laser pumping, flashlamp pumping, electric pumping, etc.

For a thin-disk solid laser, laser pumping is commonly adopted. The pumping process can be summarized as [21, Ch. 9]: i) the electrical power P_{in} to the pump laser power with the pump efficiency η_P; ii) the pump laser power to the gain absorption power with the pump light absorption efficiency η_κ; iii) the absorption power to the power stored in the upper laser level inside the gain medium P_{avail} with the quantum defect η_u. In this case, the excitation efficiency can be expressed as

$$\eta_{excit} = \eta_P \eta_\kappa \eta_u. \tag{20}$$

For homogeneously broadened lasers, the power transferred into the upper laser level can also be depicted as [21, Eq. (10.9)]

$$P_{avail} = A_g I_S g_0 \ell, \tag{21}$$

where A_g is the cross-sectional area of the gain medium. Thus, $g_0\ell$ in (18) can be depicted from (19), (20), and (21) as the following relationship with input power P_{in}:

$$g_0\ell = \frac{\eta_{excit} P_{in}}{A_g I_S}. \tag{22}$$

B. Path Loss in Mobile Transmission Channel

In the mobile transmission channel of SMIPT, the intra-cavity resonant beam intensity will increase through forward and backward passing the gain medium, and decrease by the diffraction losses (loss factor V), scattering, absorption inside the medium (loss factor V_S), and output coupling during a roundtrip. The diffraction loss is dominant to the path loss during long-range transmission in SMIPT.

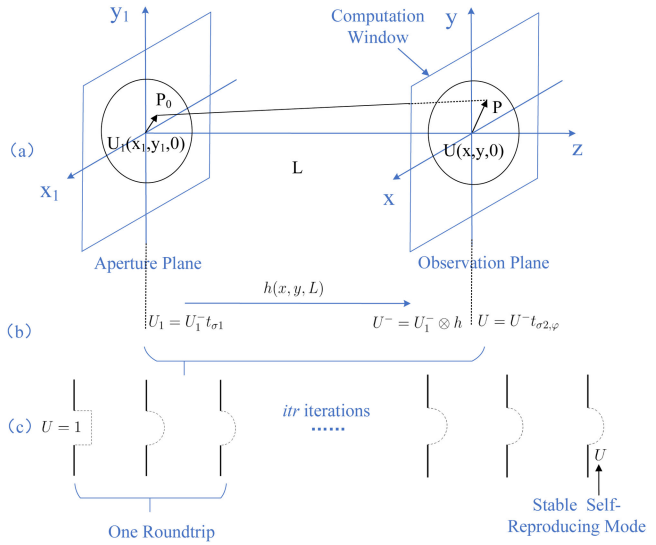

Fig. 8. Illustration of diffraction theory and self-reproducing mode calculation.

Thus, the loss factor of path loss in the SMIPT system can be depicted as

$$V = \frac{|U(x,y)|^2}{|U_1(x_1,y_1)|^2}. \tag{23}$$

Adopting the left and right CCR's equivalent planes for field calculation, $U_1(x_1, y_1)$ and $U(x, y)$ represent the self-consistent fields (i.e., self-reproducing modes of the resonator) on the equivalent planes.

We develop the solution for the self-consistent field calculation based on the Fresnel-Kirchhoff diffraction theory and Fox-Li method [22], [23]. As illustrated in Fig. 8 (a), if the field on the aperture plane is known, the field on the observation plane after free-space propagation can be calculated. Moreover, the fields before and after passing through the CCR's front face $U^-(x, y)$ and $U(x, y)$ have the following relationship [19, Eq. (1)]:

$$U(x,y) = t(x,y) \cdot U^-(x,y), \tag{24}$$

where $t(x, y)$ represents the active reflecting area of the CCR, expressed as (7) and (17).

We adopt Fast-Fourier-Transform (FFT) method for high-speed numerical calculation [24]. Double the field transmission in one propagation as shown in Fig. 8 (b), the self-consistent integral formula for one roundtrip field transmission can be derived from (24) and [24, Eq. (10)] as

$$\begin{aligned} U(x,y,L) = \mathscr{F}^{-1}\{\mathscr{F}\{\mathscr{F}^{-1}\{\mathscr{F}\{U(x,y,L)\cdot t_{\sigma 2,\varphi}(x,y)\}\cdot \\ \mathscr{F}\{h(x_1,y_1)\}\}\cdot t_{\sigma 1}(x_1,y_1)\}\cdot \mathscr{F}\{h(x,y)\}\}\cdot \\ t_{\sigma 2,\varphi}(x,y), \end{aligned} \tag{25}$$

Authorized licensed use limited to: Wenzhou University. Downloaded on June 15,2021 at 09:28:02 UTC from IEEE Xplore. Restrictions apply.

where $\mathscr{F}$ and $\mathscr{F}^{-1}$ denote the Fourier transform and inverse Fourier transform process, respectively. $h(x, y)$ named as impulse response can be expressed as [24, Eq. (7)]

$$h(x,y) = \frac{\exp(ikL)}{i\lambda L} \exp\left[\frac{ik}{2\tilde{}L}\left(x^2+y^2\right)\right], \tag{26}$$

where L is the resonator length, $k = 2\pi/\lambda$ is the wave number, λ is wavelength of resonant beam.

Using Fox-Li method [23], we can finally obtain the self-consistent field through iterating (25) itr times. As in Fig. 8 (c), the original field on the right CCR's equivalent plane $U(x, y, L) = 1$. During iterations, the field is gradually stable and eventually, the self-reproducing mode is formed. Subsequently, V can be computed.

With the self-reproducing mode, we can also determine the beam spot size A_s using the method for determining Gaussian beam radius. Gaussian beam radius w_0 is defined as the radial distance from the beam center to where the irradiance drops to $1/e^2$ of the value at the center [25, Sec. 3]. Thus, the beam spot size $A_s = \pi w_0^2$. Then, the overlapping area of the resonant beam and gain medium A_b is

$$A_b = A_s / \cos\sigma_1. \tag{27}$$

C. Laser Power Output At the Receiver

Experiencing the loss inside the gain medium, diffraction loss during transmission, and the output coupling loss, the output laser power P_{out} can be extracted from P_{avail} with the extraction efficiency η_{extr} expressed as [21, Eq. (10.11)]

$$\eta_{extr} = \frac{A_b}{A_g} \frac{(1-R)V}{1 - RV^2 + \sqrt{R}V\left[1/(V_S V) - V_S\right]}. \tag{28}$$

The small-signal gain $g_0\ell$ has to exceed the laser threshold so that the laser oscillation can be established. In our settings, the laser threshold condition is depicted as [21, Eq. (9.11)]

$$g_0\ell = \left|\ln\left(\sqrt{R}V_s V\right)\right|. \tag{29}$$

Thus, P_{in} is supposed to exceed a certain value so that the laser can be generated. Finally, (18) can be rewritten as the relationship between input and output electrical power from (22), (28), and (29) as

$$\begin{aligned} P_{out} &= A_b I_S \frac{(1-R)V}{1 - RV^2 + \sqrt{R}V\left[1/(V_S V) - V_S\right]} \times \\ &\quad \left[\frac{\eta_{exict} P_{in}}{A_g I_S} - \left|\ln\left(\sqrt{R}V_S V\right)\right|\right] \\ &= \eta_{extr}\left(\eta_{excit} P_{in} - C\right), \end{aligned} \tag{30}$$

where $C = A_g I_S |\ln(\sqrt{R}V_s V)|$. V and A_b can be obtained from (25) and (27) through the numerical calculation in Section IV. B. Thus, the energy transfer relationship between P_{out} and P_{in} can be depicted analytically as (30).

D. Energy Harvesting and Data Receiving

As in [5], the output laser power is split into two streams. One stream is for energy transfer and the other is for communication. We denote μ as the spilt ratio. Here we use the PV cell to convert the laser power into electricity for charging batteries, and adopt the APD for signal receiving. Fig. 9 depicts the basic equivalent circuit model of PV for energy harvesting. At the maximum power point, the output current $I_{pv,o}$ of the PV panel can be described as [5, Eq. (17)]

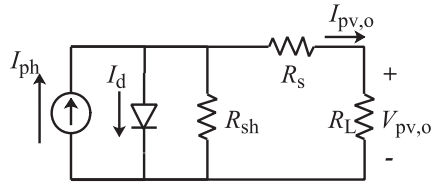

Fig. 9. Equivalent Circuit of PV for Energy Harvesting.

$$I_{pv,o} = I_{ph} - I_0(e^{c_1(V_{pv,o}+I_{pv,o}R_s)}) - \frac{V_{pv,o} + I_{pv,o}R_s}{R_{sh}}, \tag{31}$$

where I_0 is the reverse saturation current, R_s represents the additional resistance due to PV's material properties, R_{sh} represents the edge leakage of the PV. $c_1 = 1/n_s n V_T$ with n_s the number of cells inside the PV panel, n the diode ideality factor, and $V_T = (KT)/q$ is the thermal voltage of the diode, with K the Boltzmanns constant and T the temperature in Kelvin. I_{ph} depends on the received laser power of the PV, which can be depicted as

$$I_{ph} = \mu\rho P_{out}, \tag{32}$$

where ρ is the conversion responsivity factor of PV. Thus, the output charging power of the PV can be obtained as

$$P_{pv,o} = I_{pv,o} V_{pv,o} = I_{pv,o}^2 R_L, \tag{33}$$

where R_L is the load resistance of the PV.

The signal current output from the APD is depicted as

$$i_d = (1-\mu)\gamma P_{out} \quad , \tag{34}$$

where γ is a constant representing the optical-to-electrical conversion responsivity of APD. Hence, we can obtain the spectral efficiency of data transfer as [26, Eq. (26)]

$$\tilde{C} = \frac{1}{2}\log\left(1 + \frac{(i_d)^2 e}{2\pi n_{\text{total}}^2}\right), \tag{35}$$

where n_{total}^2 is the power of an Additive White Gaussian Noise (AWGN) that is the sum of contributions from shot noise and thermal noise:

$$n_{\text{total}}^2 = n_{\text{shot}}^2 + n_{\text{thermal}}^2. \tag{36}$$

The shot noise variance and thermal noise variance are specified as in [27, Eq. (12) and (14)]

$$n_{\text{shot}}^2 = 2q(i_d + I_{\text{bg}})B_x, \tag{37}$$

$$n_{\text{thermal}}^2 = \frac{4KTB_x}{R_{pd,L}}, \tag{38}$$

where q is the electron charge, B_x is the noise bandwidth, I_{bg} is the background current, and $R_{pd,L}$ is the load resistor.

V. Numerical Analysis and Discussion

In this section, we numerically analyzed the moving range, charging power, and data transfer capability of the SMIPT system. As in Sec III, we reduced the six degrees of freedom to resonator cavity length, pan angle, tilt angle, and rotation

Authorized licensed use limited to: Wenzhou University. Downloaded on June 15,2021 at 09:28:02 UTC from IEEE Xplore. Restrictions apply.

TABLE I
PARAMETER OF RESONANT BEAM

Parameter	Symbol	Value
CCR radius	r	3mm
CCR edge width	w	0.018mm
Resonant beam wavelength	λ	1.064×10^{-6}m
Output coupler reflectivity	R	0.8
Medium saturated intensity	I_s	1.26×10^{7}W/m^2
Loss factor in medium	V_s	0.99
Excitation efficiency	η_{excit}	0.5148

TABLE II
PARAMETER OF ENERGY AND DATA TRANSFER

Parameter	Symbol	Value
Conversion responsivity of PV	ρ	0.0136A/W
Reverse saturation current	I_0	9.967×10^{-8}
Diode ideality factor	n	2.5
Number of PV cell	n_s	40
Series resistance	R_s	0.93Ω
Shunt resistance	R_{sh}	52.6kΩ
Load resistor of PV	R_L	270Ω
Responsivity of APD	γ	0.6A/W [28]
Electronic charge	q	1.6×10^{-19}C
Noise bandwidth	B_x	811.7 MHz [29]
Background current	I_{bg}	5100μA [30]
Boltzmann constant	K	1.38×10^{-23}
Temperature in Kelvin	T	300K
Load resistor of APD	$R_{pd,L}$	10KΩ [27]

TABLE III
PARAMETER OF FOX-LI AND FFT ALGORITHM

Parameter	Symbol	Value
FoxLi iteration number	itr	300
Sampling number	S_N	1024
Computation window expand factor	G	2

angle. Thus, we evaluated the SMIPT performances under these movement factors with different input power.

A. Parameters

The parameters of the gain medium are from an example of a diode-end-pumped Nd:YVO_4 laser in [21], [31]. We choose the infrared beam with a wavelength of 1064 nm. Here we adopt a multi-junction PV cell where the parameters are from measured data [32]. Moreover, we specify the resonant beam parameters, energy and data transfer parameters including parameters of PV equivalent circuit, and FFT and Fox-Li algorithm parameters in Table I, II, and III, respectively.

For the FFT numerical calculation, the calculation plane and the impulse response function need to be sampled first, and the sampling number S_N is generally a power of 2. Moreover, zero-padding is needed to avoid aliasing effects as in Fig. 8. The computation window length $2Gr$ is defined as the length of zero-padded aperture, where G is the computation window expand factor, and r is the front face radius of CCR.

B. Moving Range of SMIPT

Before the moving range of the system is analyzed, we at first find out the best output coupler reflectivity. The reflectivity of the CCR at the receiver affects the output laser power of SMIPT. Thus, as in Fig. 10, we depict the output power as a function of output coupler reflectivity R with input power $P_{in} = 350$W under various pan angles θ. The best coupler reflectivity is marked with stars, which are between 0.75 and 0.8. Therefore, we choose the reflectivity $R = 0.8$ in the following evaluation.

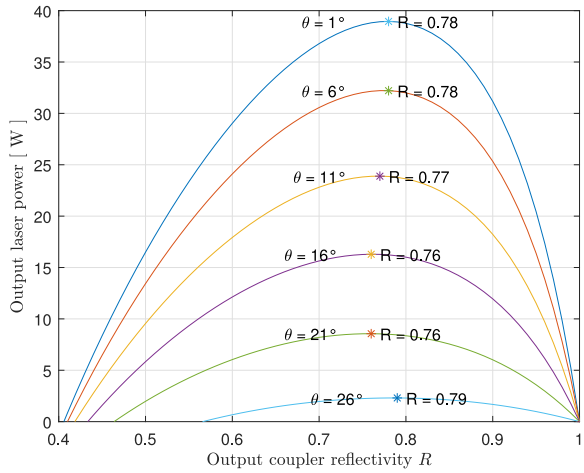

Fig. 10. Output power as a function of output coupler reflectivity R with input power $P_{in} = 350$W and various pan angle θ.

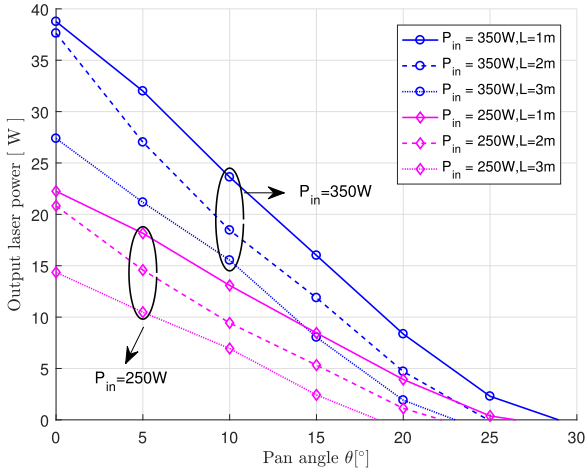

Fig. 11. Output power as a function of pan angle θ with input power $P_{in} =$ 250W and 350 W and cavity length $L =$ 1m, 2 m, and 3 m.

We define the maximum moving angle as the largest angle leading to non-zero output laser power. If the front face radius of the two CCRs is 3 mm, we choose the input power $P_{in} = 250$W and 350 W to evaluate the output power change as a function of pan angle θ, with the cavity length $L = 1$m, 2 m, and 3 m, respectively. In Fig. 11, the output power reduces as the pan angle increases.

We found that increasing input power leads to the maximum pan angle increasing. For example, when $L = 1$m, the maximum pan angles are 26° and 29° with input power 250 W and 350 W, respectively. Similar trends are also shown for the cavity length L 2 m and 3 m. Moreover, as the cavity length increases, the maximum pan angle of SMIPT decreases. The maximum angles are reduced to 25° and 23° when cavity length improves to 2 m and 3 m with input power 350 W. With a 3 m cavity length and

Authorized licensed use limited to: Wenzhou University. Downloaded on June 15,2021 at 09:28:02 UTC from IEEE Xplore. Restrictions apply.

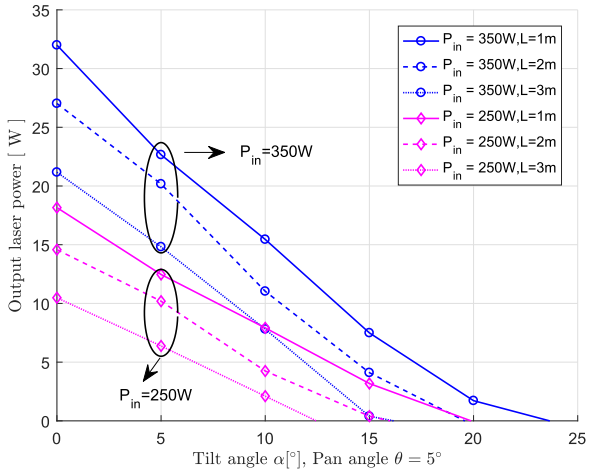

Fig. 12. Output power as a function of tilt angle α as the pan angle θ is 5° with input power $P_{in} = 250$W and 350 W and cavity length $L = 1$m, 2 m, and 3 m.

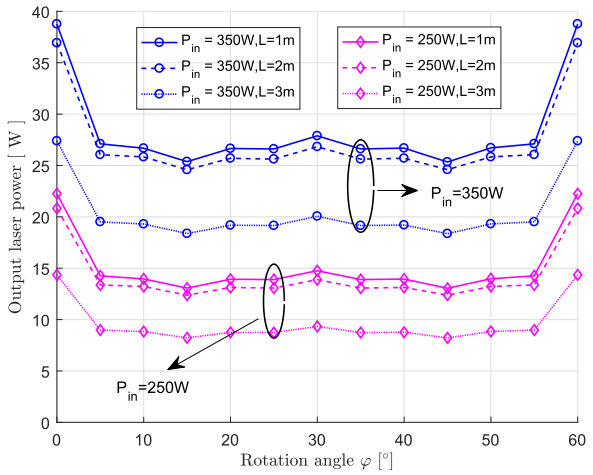

Fig. 13. Output power as a function of rotation angle φ in $[0°, 60°]$ with input power $P_{in} = 250$W and 350 W and cavity length $L = 1$m, 2 m, and 3 m.

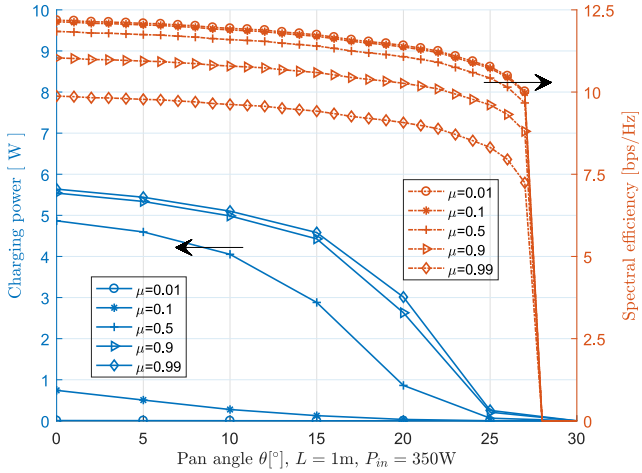

Fig. 14. Charging power and spectral efficiency as a function of pan angle θ when ratio μ is 0.01, 0.1, 0.5, 0.9, and 0.99 with input power $P_{in} = 350$W and cavity length $L = 1$m.

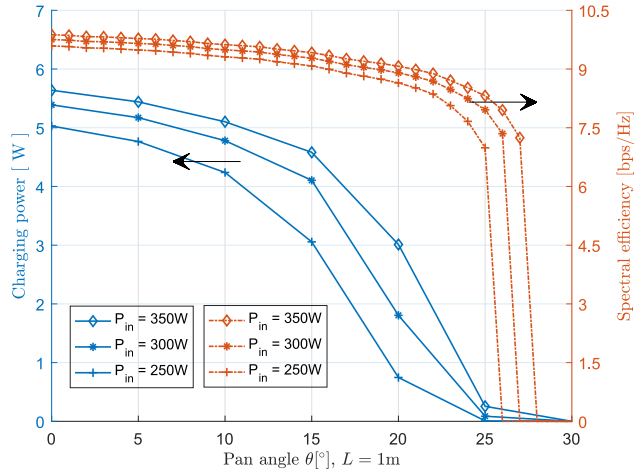

Fig. 15. Charging power and spectral efficiency as a function of pan angle θ when input power $P_{in} = 250$W, 300 W, and 350 W with ratio $\mu = 0.99$ and cavity length $L = 1$m.

250 W input power, the maximum pan angle of SMIPT system is less than 20°.

We also did the numerical analysis to find out the relationship between output power with the tilt angle α of the remote CCR. As shown in Fig. 12, the output power depicts a downtrend with the increase of the remote CCR's tilt angle. When the pan angle remains 5°, the maximum tilt angles are around 20° and 24° under 250 W and 350 W input power when the cavity length is 1 m, respectively. Same experiments have been done at the cavity length of 2 m and 3 m. As presented before, a larger cavity length leads to a smaller maximum moving angle.

To find out the impacts of rotation angle φ on output power, we evaluate the output power as the rotation angle increases every 5° in $[0°, 60°]$. In Fig. 13, if the remote CCR rotates 5°, the output power reduces around 10 W. Since the edge of the CCR cannot reflect back lights, the rotation of one of the CCR will cause more diffraction loss. Moreover, we noticed that the output power values are symmetric about the rotation angle 30°.

C. Energy-Data Transfer Performance of SMIPT

Using the parameters given in Table II, we did calculations to evaluate the wireless charging power as well as the spectral efficiency. Fig. 14 depicts how the charging power and spectral efficiency vary with the pan angle for split ratio as 0.01, 0.1, 0.5, 0.9, and 0.99. The input power is 350 W and the cavity length is 1 m. With the increase of split ratio, the charging power enhances while the spectral efficiency reduces. Moreover, SMIPT can realize multi-Watt wireless charging as well as up to ten bps/Hz spectral efficiency for data transfer with room-range mobility. To achieve more charging power, we choose the split factor 0.99 to do more evaluation.

In Fig. 15, we present the relationship of the SMIPT performance with the system input power. The cavity length remains as 1 m. Then, the energy and data transfer performance and maximum pan angle increase as the input power increases. Moreover, a larger pan angle leads to worse performance for both wireless charging and data transfer.

Authorized licensed use limited to: Wenzhou University. Downloaded on June 15,2021 at 09:28:02 UTC from IEEE Xplore. Restrictions apply.

TABLE IV
COMPARISON OF EXISTING SLIPT SCHEMES

Scheme	Input power	Harvested Energy	Data Transfer	Moving range
Laser-based, Fakidis *et al.*[9]	not mentioned	192mW	2.9bps/Hz SE	2m distance without mobility
Laser-based, Fakidis *et al.*[10]	282mW	1.8mW	not stated	5.2m distance without mobility
VLC-based, Ma *et al.*[5]	316.2W	2.96mW	6bps/Hz data rate	120-degree FOV, 1.5m distance
VLC-based, Abdelhady *et al.* [6]	450W	0.38mW	8bps/Hz SE	3m× 3m room size, 3m height
VLC-based, Wang *et al.*[7]	not mentioned	30mW	11.84Mbps data rate	120-degree FOV, 0.75m distance
VLC-based, Diamantoulakis *et al.* [4]	400W	1.9mJ	7bps/Hz data rate	120-degree FOV, 1.5m distance
SMIPT	350W	5W	9.5bps/Hz	40-degree FOV, 3m distance

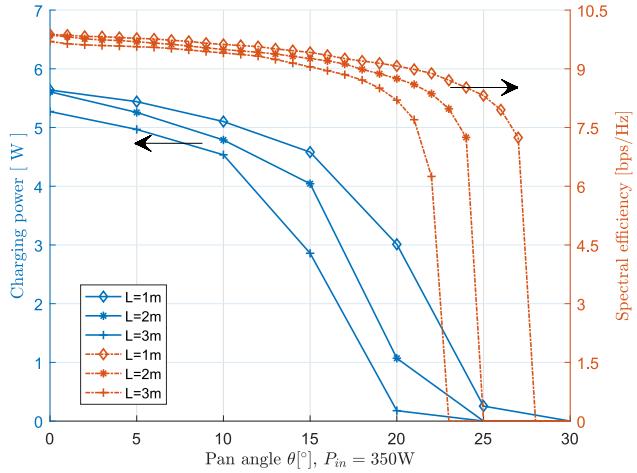

Fig. 16. Charging power and spectral efficiency as a function of pan angle θ when the cavity length is $L = 1$m, 2 m, and 3 m with input power $P_{in} = 350$W and ratio $\mu = 0.99$.

Finally, we analyze the relationship of the SMIPT performance with the cavity length, i.e., the distance between SMIPT transmitter and receiver. In Fig. 16, the performances of both energy and data transfer become poorer as the cavity length increases. However, when the pan angle is below 20°, the spectral efficiency doesn't change much. The maximum pan angles are around 23°, 25°, and 28° when the cavity length is 1 m, 2 m, and 3 m, with 350 W input power, respectively.

D. Summary

In summary, this numerical evaluation demonstrated that SMIPT is capable of delivering more than 5 W charging power and enabling 9.5 bps/Hz spectral efficiency for data transfer, with 40-degree FoV under 350 W input power and 3 m transmission distance. Besides, we reviewed the energy/data transfer and mobility performance of the related SLIPT schemes to highlight the performance with the proposed SMIPT system. Table IV depicts the optimal performance indicators which are satisfied simultaneously of the existing SLIPT systems. SMIPT has advantages in providing high charging power, while simultaneously enabling high spectral efficiency and a large moving range.

VI. DISCUSSION

A. Moving Speed Impacts

Besides, moving speed also has impacts on SMIPT stability and performance. SMIPT relies on RBS to form a new design of transmission channel. The impacts of moving speed on SMIPT performance have not been well analyzed, which is important for application scenarios where the receivers are continuously moving. Thus, we illustrate the fundamentals on the re-buildup time of RBS after receivers' moving below to provide guidelines for future study on moving speed impact.

RBS is essentially an open-cavity laser system, of which the pumping process can be described with the four-level rate equation model [21, Ch. 9]. The inverted population density in a four-level system can be depicted as [21, Eq. (9.31)]

$$\frac{\mathrm{d}\Delta n(t)}{\mathrm{d}t} = -\Delta n(t)(\sigma_{21}\nu + A_{21}) + [n - \Delta n(t)]W_{03}, \quad (39)$$

where σ_{21} is the stimulated emission cross section, A_{21} is the spontaneous emission probability, ν is the resonance mode frequency, W_{03} is the pump power, and n is the atomic density in the gain medium. The solution to (39) as the threshold is nearly reached is:

$$\Delta n(t) = B\mathrm{e}^{-(A_{21}+w_{03})t} + \frac{nW_{03}}{A_{21}+W_{03}}\mathrm{e}^{-(A_{21}+W_{03})t} \times \left[\mathrm{e}^{(A_{21}+W_{03})t} - 1\right]. \quad (40)$$

Assume the pump start time $t = 0$, then B can be depicted as

$$B = n\left(\mathrm{e}^{-\frac{E_2}{KT_{op}}} - \mathrm{e}^{-\frac{E_1}{KT_{op}}}\right), \quad (41)$$

where E_1 and E_2 are the lower-level energy and upper-level energy of the laser gain medium, respectively; K is the Boltzmann constant, and T_{op} is the laser operation temperature in Kelvin.

Then, the self-oscillation condition can be expressed as

$$\Delta n(t) = \frac{\delta}{\sigma_{21} l}, \quad (42)$$

where δ is the one-way loss factor and l is the length of the gain medium. Substitute (40) and (41) to (42), then we can obtain the buildup time for the RBS as

$$t = -\frac{\ln\left[\dfrac{\frac{\delta}{\sigma_{21}l} - \frac{nW_{03}}{A_{21}+W_{03}}}{n\left(\mathrm{e}^{-\frac{E_2}{KT_{op}}} - \mathrm{e}^{-\frac{E_1}{KT_{op}}}\right) - \frac{nW_{03}}{A_{21}+W_{03}}}\right]}{A_{21}+W_{03}}. \quad (43)$$

Given the parameters for Nd:YVO $_4$ gain medium as follows: $n = 1.37 \times 10^{20}$ atoms/cm ^{3}, $\sigma_{21} = 25 \times 10^{-19}$ cm^2, $T_{op} = 310$K, $A_{21} = 10^4$s $^{-1}$, $\exp(-E_2/KT_{op}) = e^{-10}$, and $\exp(-E_1/KT_{op}) = e^{-11}$, we plot the buildup time of RBS as the pan angle θ increases with the input power 250 W, 300 W, and 350 W and cavity length 3 m. As in Fig. 17, during the moving process of the receiver, the buildup time of the RBS, i.e., transmission channel in the SMIPT, is below 110μ s within the moving range. Moreover, the buildup time decreases as the input power grows up. Even though the transmission channel is broken

Authorized licensed use limited to: Wenzhou University. Downloaded on June 15,2021 at 09:28:02 UTC from IEEE Xplore. Restrictions apply.

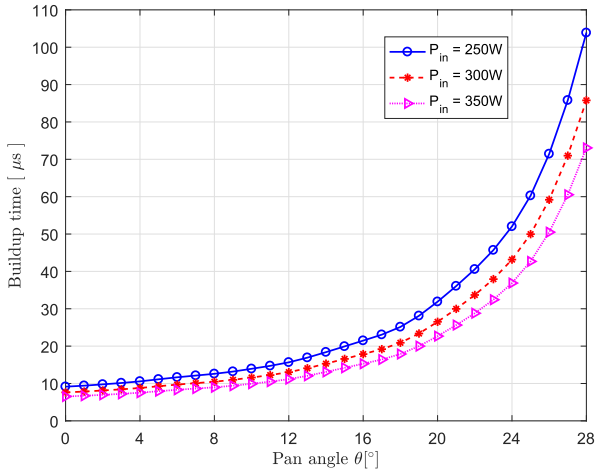

Fig. 17. Buildup time of the RBS as a function of pan angle θ when the cavity length is $L = 3$m with input power $P_{in} = 250300$, and 350 W.

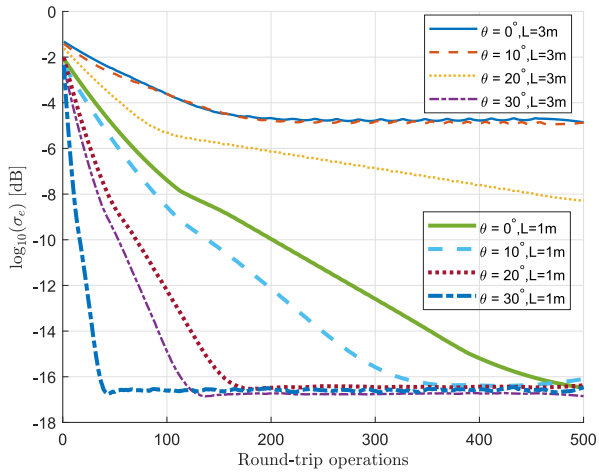

Fig. 18. Convergence velocity of the system under various pan angles θ with cavity length $L = 1$m and $L = 3$m.

during the moving, the channel can be rebuilt in around tens of μs. If the transmission channel is not broken, the transmission speed of the resonant beam is equal to the speed of light. Thus, as the maximum moving speed of a human is 44 m/s [33], the performance fluctuation can be neglected during the moving process. Methods for maintaining the stability are worth in-depth studying.

B. Computational Complexity Analysis

Calculating the self-reproducing field is the most time-consuming part of obtaining the mobile transmission channel loss and then the output laser power to analyze the system performance. Thus, we evaluate here the computational complexity and convergence of the adopted methods, i.e., Fresnel-Kirchoff's diffraction formula depicting one round-trip transmission and Fox-Li method for obtaining the self-reproducing field distribution.

1) Computational Complexity of One Round-Trip Transmission: According to [24], functions in (25) should be sampled at first. Thus, $U(x, y, L)$, $h(x, y)$, $t_{\sigma 1}(x, y)$, and $t_{\sigma 2,\varphi}(x, y)$ are given as matrices $\mathbf{U}$, $\mathbf{H}$, $\mathbf{T}_1$, and $\mathbf{T}_2$, respectively. Then, the computational load of one round-trip resonant beam transmission as in (25) comes from

- calculation and generation of $\mathbf{T}_2$;
- element-by-element multiplication $\mathbf{A} = \mathbf{U} \cdot \mathbf{T}_2$;
- an FFT process as $\mathscr{F}\{\mathbf{A}\}$;
- calculation and generation of $\mathbf{H}$;
- $\mathscr{F}\{\mathbf{H}\}$;
- $\mathbf{B} = \mathscr{F}\{\mathbf{A}\} \cdot \mathscr{F}\{\mathbf{H}\}$;
- an inverse FFT (IFFT) process as $\mathscr{F}^{-1}\{\mathbf{B}\}$;
- calculation and generation of $\mathbf{T}_1$;
- $\mathbf{C} = \mathscr{F}^{-1}\{\mathbf{B}\} \cdot \mathbf{T}_1$;
- $\mathscr{F}\{\mathbf{C}\}$;
- $\mathbf{D} = \mathscr{F}\{\mathbf{C}\} \cdot \mathscr{F}\{\mathbf{H}\}$;
- $\mathscr{F}^{-1}\{\mathbf{D}\}$;
- $\mathbf{E} = \mathscr{F}^{-1}\{\mathbf{D}\} \cdot \{\mathbf{T}_2\}$.

Thus, three matrix generation operations, five element-by-element multiplication operations, three FFT operations, and two IFFT operations are included in the above calculation. Given a sampling number S_N (i.e., the matrix size is $S_N \times S_N$), the computational complexity of one round-trip transmission is expressed as

$$\begin{aligned} C &= 3C_{\text{gen}} + 5C_{\text{mul}} + 3C_{\text{fft}} + 2C_{\text{ifft}} \\ &= 3O(S_N^2) + 5O(S_N^2) + 3O(S_N^2 \log_2 S_N) \\ &\quad + 2O(S_N^2 \log_2 S_N) \\ &= 8O(S_N^2) + 5O(S_N^2 \log_2 S_N). \end{aligned} \tag{44}$$

S_N is the key to the computational load and it should satisfy $S_N \gg 4r^2/\lambda/L$ [34]. More sampling points are needed for a larger CCR's front face size and smaller cavity length, and the value 1024 we choose meets the above requirement.

2) Convergence of the Fox-Li Method: As illustrated in Sec. IV-B, we use the Fox-Li method to calculate the self-reproducing filed for evaluating the path loss, i.e., iterating (25) multiple times until a stable field is formed. The convergence of the Fox-Li method relying on the resonator parameters impacts the time of the path loss calculation. Thus, we analyze the convergence of Fox-Li here with the resonator parameters in our settings. The convergence is examined by comparing the normalized field distribution with the normalized one after the last round-trip transmission (i.e., the last iteration). The error estimated as the amount of difference between the two field distribution after itr iterations is depicted as

$$\mathbf{\Delta}_{itr} = \mathbf{U}_{itr} - \mathbf{U}_{itr-1}. \tag{45}$$

Then we use the standard deviation σ_e of the error to depict the convergence velocity and the target derivation is 10^{-4} [35]. Fig. 18 shows the convergence velocity with 1 m and 3 m transmission distances and various pan angles. The convergence velocity increases with the increase of pan angle θ and cavity length L. That's because as θ or L increases, the Fresnel number of the resonator which determined by size of reflector and cavity length reduces, while larger Fresnel number makes the

Authorized licensed use limited to: Wenzhou University. Downloaded on June 15,2021 at 09:28:02 UTC from IEEE Xplore. Restrictions apply.

convergence of Fox-Li method worse. As in Fig. 18, in all cases in our simulation the target convergence can be achieved within 200 round-trip operations. Moreover, accelerated methods for obtaining self-consistent field in resonators with high Fresnel number have emerged [35], [36], which can be deeply studied and applied in the future work.

3) Calculation Speed: We run our simulation in MATLAB using a personal computer with an Intel Core i5, 2.4 GHz CPU and 8 GB RAM to investigate the speed for calculating the self-consistent field. The execution time of one round-trip transmission with a 1024×1024 sampling array is around 0.3 s. It means that we can obtain a result within 100 s. Besides, GPU can be exploited to accelerate the FFT operation and element-by-element multiplication operation if larger sampling array is required due to its excellent performance in parallel computing for matrix operations, which is worthy of further investigation.

VII. Conclusion

In this paper, we proposed an SMIPT approach which can achieve energy-concentrated narrow beam transmission and self-alignment of the mobile receiver simultaneously. We depicted the system design relying on the RBS and illustrated its characteristics of high-power, safety, and mobility. We established a geometric model of mobile transmission channel to reveal the mobility mechanism and an analytical model of mobile energy and information transfer to quantitatively evaluate the SMIPT performance (moving range, charging power, and spectral efficiency). The numerical analysis highlighted the superior performance of SMIPT, which showed its advantage in providing high charging power over large moving range compared with the existing SLIPT benchmarks. Moreover, we discussed the re-buildup time of transmission channel after receiver's moving to provide fundamentals for study on moving speed impacts. SMIPT is a practical solution for realizing mobile energy supply and data transfer.

Several interesting topics are worthy of investigation in the future: 1) method for maintaining SMIPT stability impacted by moving speed; 2) design and analysis for the long distance, e.g., hundreds-of-meters, transfer and multiple receivers; and, 3) methods of dealing with non-line-of-sight (NLOS), e.g. adopting intelligent reflecting surface (IRS).

References

[1] K. David and H. Berndt, "6G vision and requirements: Is there any need for beyond 5G?," *IEEE Veh. Technol. Mag.*, vol. 13, no. 3, pp. 72–80, Sep. 2018.

[2] X. Liu, Y. Wang, F. Zhou, S. Ma, R. Q. Hu, and D. W. K. Ng, "Beamforming design for secure MISO visible light communication networks with SLIPT," *IEEE Trans. Commun.*, vol. 68, no. 12, pp. 7795–7809, Aug. 2020.

[3] *Key Technologies for 5G Wireless Systems*. Cambridge, U.K.: Cambridge Univ. Press, 2017.

[4] P. D. Diamantoulakis, G. K. Karagiannidis, and Z. Ding, "Simultaneous lightwave information and power transfer (SLIPT)," *IEEE Trans. Green Commun. Netw.*, vol. 2, no. 3, pp. 764–773, Sep. 2018.

[5] S. Ma, F. Zhang, H. Li, F. Zhou, Y. Wang, and S. Li, "Simultaneous lightwave information and power transfer in visible light communication systems," *IEEE Trans. Wireless Commun.*, vol. 18, no. 12, pp. 5818–5830, Dec. 2019.

[6] A. M. Abdelhady, O. Amin, B. Shihada, and M. Alouini, "Spectral efficiency and energy harvesting in multi-cell slipt systems," *IEEE Trans. Wireless Commun.*, vol. 19, no. 5, pp. 3304–3318, Feb. 2020.

[7] Z. Wang, D. Tsonev, S. Videv, and H. Haas, "On the design of a solar-panel receiver for optical wireless communications with simultaneous energy harvesting," *IEEE J. Sel. Areas Commun.*, vol. 33, no. 8, pp. 1612–1623, Aug. 2015.

[8] G. Pan, J. Ye, and Z. Ding, "Secure hybrid VLC-RF systems with light energy harvesting," *IEEE Trans. Commun.*, vol. 65, no. 10, pp. 4348–4359, Oct. 2017.

[9] J. Fakidis, S. Videv, H. Helmers, and H. Haas, "0.5-Gb/s OFDM-based laser data and power transfer using a GaAs photovoltaic cell," *IEEE Photon. Technol. Lett.*, vol. 30, no. 9, pp. 841–844, May 2018.

[10] J. Fakidis, S. Kucera, H. Claussen, and H. Haas, "On the design of a free space optical link for small cell backhaul communication and power supply," in *Proc. IEEE Int. Conf. Commun. Workshop*, London, U.K., Jun. 2015, pp. 1428–1433.

[11] Q. Liu *et al.*, "Charging unplugged: Will distributed laser charging for mobile wireless power transfer work?," *IEEE Veh. Technol. Mag.*, vol. 11, no. 4, pp. 36–45, Dec. 2016.

[12] M. Xiong, Q. Liu, M. Liu, X. Wang, and H. Deng, "Resonant beam communications with photovoltaic receiver for optical data and power transfer," *IEEE Trans. Commun.*, vol. 68, no. 5, pp. 3033–3041, May 2020.

[13] W. Wang, Q. Zhang, H. Lin, M. Liu, X. Liang, and Q. Liu, "Wireless energy transmission channel modeling in resonant beam charging for IoT devices," *IEEE Internet Things J.*, vol. 6, no. 2, pp. 3976–3986, Apr. 2019.

[14] J. Lim, T. S. Khwaja, and J. Ha, "Wireless optical power transfer system by spatial wavelength division and distributed laser cavity resonance," *Opt. Exp.*, vol. 27, no. 12, p. A 924, Jun. 2019.

[15] D. A. Arnold, "Method of calculating retroreflector-array transfer functions," *SAO Special Rep.*, vol. 382, Feb. 1979.

[16] G. Zhou, A. J. Alfrey, and L. W. Casperson, "Modes of a laser resonator with a retroreflecting corner cube mirror," *Appl. Opt.*, vol. 21, no. 9, pp. 1670–1674, May 1982.

[17] T. Takatsuji, M. Goto, S. Osawa, R. Yin, and T. Kurosawa, "Whole-viewing-angle cat's-eye retroreflector as a target of laser trackers," *Meas. Sci Technol.*, vol. 10, no. 7, pp. N 87–N90, Jan. 1999.

[18] M. Murray-Lasso, "On the generalization of the law of cosines of triangles to three and more dimensions," *Ingeniera Investigacin y Tecnologa*, vol. 3, no. 4, pp. 169–183, Oct. 2002.

[19] M. Shen, S. Wang, L. Hu, and D. Zhao, "Mode properties produced by a corner-cube cavity," *Appl. Opt.*, vol. 43, no. 20, pp. 4091–4094, Apr. 2004.

[20] B. Dubrovin, A. Fomenko, and S. Novikov. *Modern Geometry-Methods and Applications: Part II: The Geometry and Topology of Manifolds*, ser. Graduate Texts in Mathematics. New York, NY, USA: Springer, 2012.

[21] N. Hodgson and H. Weber, *Laser Resonators and Beam Propagation: Fundamentals, Advanced Concepts, Applications, Ser. Springer Series in Optical Sciences*. Berlin Heidelberg, Germany: Springer, 2005, vol. 108.

[22] J. A. Hudson, "Fresnel-kirchhoff diffraction in optical systems: An approximate computational algorithm," *Appl. Opt.*, vol. 23, no. 14, pp. 2292–2295, Jul. 1984.

[23] A. G. Fox and T. Li, "Resonant modes in a maser interferometer," *Bell System Tech. J.*, vol. 40, no. 2, pp. 453–488, Mar. 1961.

[24] F. Shen and A. Wang, "Fast-Fourier-transform based numerical integration method for the Rayleigh-Sommerfeld diffraction formula," *Appl. Opt.*, vol. 45, no. 6, pp. 1102–1110, Feb. 2006.

[25] M. González-Cardel, P. Arguijo, and R. Díaz-Uribe, "Gaussian beam radius measurement with a knife-edge: A polynomial approximation to the inverse error function," *Appl. Opt.*, vol. 52, no. 16, pp. 3849–3855, Jun. 2013.

[26] A. Lapidoth, S. M. Moser, and M. A. Wigger, "On the capacity of free-space optical intensity channels," *IEEE Trans. Inf. Theory*, vol. 55, no. 10, pp. 4449–4461, Oct. 2009.

[27] F. Xu, M. Khalighi, and S. Bourennane, "Impact of different noise sources on the performance of PIN- and APD-based FSO receivers," in *Proc. 11th Int. Conf. Telecommun.*, Graz, Austria, Jun. 2011, pp. 211–218.

[28] M. S. Demir, F. Miramirkhani, and M. Uysal, "Handover in VLC networks with coordinated multipoint transmission," in *Proc. IEEE Int. Black Sea Conf. Commun. Netw.*, Istanbul, Turkey, Jun. 2017, pp. 1–5.

[29] C. Quintana *et al.*, "High speed electro-absorption modulator for long range retroreflective free space optics," *IEEE Photon. Technol. Lett.*, vol. 29, no. 9, pp. 707–710, Mar. 2017.

[30] A. Moreira, R. Valadas, and A. M. De Oliveira Duarte, "Optical interference produced by artificial light," *Wireless Netw.*, vol. 3, no. 2, pp. 131–140, May 1997.

Authorized licensed use limited to: Wenzhou University. Downloaded on June 15,2021 at 09:28:02 UTC from IEEE Xplore. Restrictions apply.

[31] P. Crump *et al.*, "100-W diode laser bars show > 71% power conversion from 790- nm to 1000-nm and have clear route to > 85%," in *Proc. SPIE, Ser. Soc. Photo-Opt. Instrum. Engineers Conf. Ser.*, vol. 6456, 2007, Art. no. 64560M.
[32] M. Perales *et al.*, "Characterization of high performance silicon-based VMJ PV cells for laser power transmission applications," in *Proc. High-Power Diode Laser Technol. Appl. XIV, Ser. Soc. Photo-Opt. Instrum. Engineers Conf. Ser.*, vol. 9733, Mar. 2016, Art no. 97330U.
[33] V. Iyer, E. Bayati, R. Nandakumar, A. Majumdar, and S. Gollakota, "Charging a smartphone across a room using lasers," *Proceedings the ACM Interactive Mobile Wearable Ubiquitous Technol.*, vol. 1, no. 4, pp. 1–21, Jan. 2018.
[34] J. Yoo, Y. U. Jeong, B. C. Lee, Y. J. Rhee, and S. O. Cho, "Numerical simulation of laser resonators," *J. Korean Phys. Soc.*, vol. 44, no. 2, pp. 293–302, Feb. 2004.
[35] D. Asoubar, M. Kuhn, and F. Wyrowski, "Acceleration of dominant transversal laser resonator eigenmode calculation by vector extrapolation methods," *IEEE J. Quantum Electron.*, vol. 51, no. 11, pp. 1–10, Nov. 2015.
[36] P. Saha, "Fast estimation of transverse fields in high-finesse optical cavities," *J. Opt. Soc. Amer. A*, vol. 14, no. 9, pp. 2195–2202, Sep. 1997.

Mingqing Liu received the B.S. degree in computer science and technology from the Northwest A&F University, Yangling, China, in 2018. She is currently working toward the Ph.D. degree with the College of Electronics and Information Engineering, Tongji University, Shanghai, China. Her research interests include wireless power transfer, development of remote wireless charging technology, and the Internet of Things.

Hao Deng received the B.S. and Ph.D. degrees from the Department of Physical Electronics, University of Electronic Science and Technology, Chengdu, China, in 2007 and 2015, respectively. He is currently an Assistant Professor with the School of Software Engineering, Tongji University, Shanghai, China. His research interests include optical critical dimension measurement for semiconductors, wireless power transfer, and Internet of Things.

Qingwen Liu (Senior Member, IEEE) received the B.S. degree in electrical engineering and information science from the University of Science and Technology of China, Hefei, China, in 2001 and the M.S. and Ph.D. degrees from the Department of Electrical and Computer Engineering, University of Minnesota, Minneapolis, MN, USA, in 2003 and 2006, respectively. He is currently a Professor with the College of Electronics and Information Engineering, Tongji University, Shanghai, China. His research interests include wireless power transfer and Internet of Things.

Jie Zhou received the B.S. degree from Nanchang University, Nanchang, China, in 2020. She is currently working toward the M.S. degree with the College of Electronics and Information Engineering, Tongji University, Shanghai, China. Her research interests include wireless power transfer, development of remote wireless charging technology, and Internet of Things.

Mingliang Xiong received the B.S. degree in communication engineering from the Nanjing University of Posts and Telecommunications, Nanjing, China, in 2017. He is currently working toward the Ph.D. degree with the College of Electronics and Information Engineering, Tongji University, Shanghai, China. His research interests include optical wireless communications, wireless power transfer, and the Internet of Things.

Liuqing Yang (Fellow, IEEE) received the Ph.D. degree in electrical and computer engineering from the University of Minnesota, Minneapolis, MN, USA, in 2004. She is currently a Professor with University of Minnesota. She has authored or coauthored more than 330 journal and conference papers, four book chapters and five books in her general interests, which includes communications and networking. She was the recipient of the ONR Young Investigator Program Award in 2007, and the NSF Faculty Early Career Development Award in 2009, the Best Paper Award at IEEE ICUWB'06, ICCC'13, ITSC'14, GLOBECOM'14, ICC'16, WCSP'16, GLOBECOM'18, ICCS'18, and ICC'19. She is the Editor-in-Chief of the *IET Communications*, Executive Editorial Committee Member of the IEEE TRANSACTIONS ON COMMUNICATIONS, and Senior Editor of the IEEE TRANSACTIONS ON SIGNAL PROCESSING. She was the Editor of the IEEE TRANSACTIONS ON WIRELESS COMMUNICATIONS, IEEE TRANSACTIONS ON INTELLIGENT TRANSPORTATION SYSTEMS, IEEE INTELLIGENT SYSTEMS, and *PHYCOM: Physical Communication*, and the Program Chair, Track or Symposium or TPC chair for many conferences.

Georgios B. Giannakis (Fellow, IEEE) received the Diploma degree in electrical engineering from the National Technical University of Athens, Athens, Greece, in 1981, the M.Sc. degree in 1983 in electrical engineering, the M.Sc. degree in 1986 in mathematics, and the Ph.D. degree in 1986 in electrical engineering from the University of the Southern California, Los Angeles, CA, USA. From 1982 to 1986, he was with the University of the Southern California, Los Angeles, CA, USA. From 1987 to 1998, he was with the University of Virginia, Charlottesville, VA, USA, and since 1999, he has been a Professor with the University of Minnesota, Minneapolis, MN, USA, where he holds an Endowed Chair of wireless telecommunications, University of Minnesota McKnight Presidential Chair of electrical and computer engineering, and the Director of the Digital Technology Center. He has authored or coauthored more than 450 journal papers, 750 conference papers, 25 book chapters, two edited books, and two research monographs (h-index 143) in his general interests, which include communications, networking, and statistical signal processing. His current research interests include learning from big data, wireless cognitive radios, and network science with applications to social, brain, and power networks with renewables. He is the co-inventor of 32 patents issued, and the co-recipient of nine best paper awards from the IEEE Signal Processing and Communications Societies, including the G. Marconi Prize Paper Award in Wireless Communications. He was also the recipient of the Technical Achievement Awards from the SP Society in 2000, from the EURASIP in 2005, the IEEE ComSoc Education Award in 2019, a Young Faculty Teaching Award, the G. W. Taylor Award for Distinguished Research from the University of Minnesota, and the IEEE Fourier Technical Field Award (inaugural recipient in 2015). He is a Fellow of the EURASIP and was with the IEEE in a number of posts, including that of a Distinguished Lecturer for the IEEE-SP Society.

Authorized licensed use limited to: Wenzhou University. Downloaded on June 15,2021 at 09:28:02 UTC from IEEE Xplore. Restrictions apply.